



ELSEVIER

Chemical
Physics

Chemical Physics 258 (2000) 371–390

www.elsevier.nl/locate/chemphys

A theoretical analysis of the sum frequency generation spectrum of the water surface

Akihiro Morita ^{a,b}, James T. Hynes ^{a,c,*}

^a Department of Chemistry and Biochemistry, University of Colorado, Boulder, CO 80309-0215, USA

^b Department of Chemistry, Graduate School of Science, Kyoto University, Kyoto 606-8502, Japan

^c Département de Chimie, CNRS UMR 8640, Ecole Normale Supérieure, 24 rue Lhomond, Paris 75231, France

Received 2 March 2000

Abstract

The present paper provides a theoretical analysis of the sum frequency generation (SFG) spectrum of the water surface in the OH stretch mode frequency region based on ab initio molecular orbital theory and molecular dynamics simulation. The environmental effects on the normal modes of OH stretching vibration, their frequency shifts and hyperpolarizability are formulated and tested. The simulated SFG spectrum reproduces experimental results quite well. The surface susceptibilities of the dangling bond and hydrogen-bonded bands have opposite signs in their imaginary parts, which indicates opposite OH directions at the surface associated with these bands. The former band turns out to be sensitive only to the top monolayer, and the latter band to a few top monolayers. Further analysis reveals that those two bands arise from quite different types of molecular orientations. The assignment of the SFG spectrum is also analyzed in terms of the symmetric/antisymmetric character of the OH stretching modes and the degree of mode delocalization. © 2000 Elsevier Science B.V. All rights reserved.

1. Introduction

The structure and dynamics at liquid/vapor interfaces, of extensive significance in a wide variety of areas [1–7], have assumed increasing importance in the past few decades in the context of heterogeneous atmospheric chemistry [8–21]. However, despite their importance, the microscopic structures of these interfaces are less well understood than their solid counterparts, mainly due to the limited number of experimental methods available for the probing of the liquid surfaces.

While the understanding of the solid surfaces has been facilitated by many sophisticated experimental techniques operative in an ultravacuum environment [22], most of these methods are not usually applicable to liquid/vapor interfaces, due to the substantial vapor pressure. Accordingly, most of the structural information so far has been provided by computer simulations [3,4,23–31]. Sum frequency generation (SFG) is a unique mode of surface vibrational spectroscopy to experimentally probe the microscopic structures of liquid surfaces [5–7,32–40]. As with the nonvibrational second harmonic generation (SHG) technique [5–7], not only is the SFG a surface-specific technique since the bulk dipole contribution cancels out by its isotropic nature [41], it is also readily applied to

*Corresponding author.

E-mail address: hynes@spot.colorado.edu (J.T. Hynes).

any interface accessible by light. As a first step towards the treatment of liquid/vapor interfaces of environmental importance, the present work deals with the theory and simulation of the SFG spectrum for water.

Although the formal theoretical framework of SFG theory has been established [32,41], the structural information involved in SFG spectra has not been thoroughly explored. Previous analyses of SFG spectra [35–37] have attempted to derive molecular orientations at surfaces with a simple assumption of orientational distributions and/or hyperpolarizability involving some empirical parameters. These efforts have produced useful, but somewhat uncertain results, the difficulty in analyzing actual SFG spectra mainly arising from the lack of microscopic expressions for molecular hyperpolarizability tensors and their dependence on molecular vibrations. In an important initial effort, Benjamin attempted to interpret the SFG spectrum of the liquid water/vapor interface by MD simulations [29], but he discussed a hypothetical infrared (IR) spectrum at the surface region instead of the actual SFG spectrum due to the above difficulties; nonetheless Benjamin pointed out the resemblance of the two spectra. Sokhan and Tildesley [31] have calculated the static nonlinear susceptibility at the water surface, but susceptibility considerations in the frequency domain are needed to simulate SFG spectra.

The present work provides a simple, convenient way to analyze the SFG spectrum of surface water using ab initio molecular orbital (MO) theory and MD simulations. While we avoid explicit simulation of the molecular vibrations to substantially simplify the analysis, our approximate treatment is useful to extract surface structural information, as shown within.

The remainder of this paper is constructed as follows. In Section 2, a model treatment of the SFG spectrum and molecular hyperpolarizability in the water OH stretching region is presented. In Section 3, the MD procedure employed is described, and the results on the surface structure are given. The SFG spectrum of water is simulated and analyzed in Section 4, and the assignment of the vibrational modes is discussed in Section 5. Concluding remarks follow in Section 6.

2. Modeling of the SFG spectrum and hyperpolarizability

2.1. Approximate expression of the SFG intensity

To begin, we consider the SFG spectrum of a liquid water/vapor interface at the frequency $\omega_{\text{SFG}} = \omega_{\text{vis}} + \omega_{\text{IR}}$, where ω_{vis} is the visible frequency fixed at a nonresonant value and ω_{IR} is the tunable infrared frequency. The combination of light polarization is either *ssp* or *sps*, where *s* and *p* are the usual notation of polarization: *s* denotes the polarization parallel to the surface, and *p* is the other component perpendicular to *s*. Each character, *s* or *p*, corresponds to the polarization of the SFG, visible and IR fields, respectively. Although the SFG intensity depends on the experimental geometry, its frequency dependence is represented by Refs. [32,34]

$$I_l(\omega_{\text{SFG}}) \propto \omega_{\text{SFG}}^2 |\chi_{lmn}(\omega_{\text{SFG}}, \omega_{\text{vis}}, \omega_{\text{IR}})|^2 I_m(\omega_{\text{vis}}) I_n(\omega_{\text{IR}}), \quad (1)$$

where $\chi_{lmn}(\omega_{\text{SFG}}, \omega_{\text{vis}}, \omega_{\text{IR}})$ is the macroscopic susceptibility of the water surface and the indices *lmn* denote the combination of the light polarizations. We neglect the nonlocal quadrupolar contribution to the nonlinear induced polarization, since it is a minor component for water compared to the surface dipolar contribution [42].

The susceptibility χ_{lmn} can be represented as a sum of resonant χ_{lmn}^r and nonresonant χ_{lmn}^{nr} components [32,34,41]: $\chi_{lmn} = \chi_{lmn}^r + \chi_{lmn}^{\text{nr}}$. Since we are interested in the vibrational structure of the SFG spectrum, we mainly deal with the resonant component χ_{lmn}^r , with the nonresonant one χ_{lmn}^{nr} treated as a constant parameter. It is microscopically represented as the average sum of first-order hyperpolarizability of the constituent molecules β in the space-fixed frame,

$$\chi_{lmn}^r = \left\langle \sum_{i(\text{molecules})}^N \sum_{pqr} D_{lp}(\Omega_i) D_{mq}(\Omega_i) D_{nr}(\Omega_i) \beta_{pqr} \right\rangle, \quad (2)$$

where the subscripts *p–r* denote body-fixed axes. $D(\Omega_i)$ is the direction cosine matrix of each *i*th molecule, projecting β onto the space-fixed frame.

The angle brackets $\langle \rangle$ of Eq. (2) denote a statistical average over the microscopic configurations. Provided that the surface normal is along the Z axis and the incident light is along the XZ plane in the space-fixed frame, the susceptibility components relevant to the ssp and sps signals are χ_{YYZ} and χ_{YZY} , respectively; thus χ_{YYZ} and χ_{YZY} in the space-fixed frame are hereafter denoted by χ_{ssp} and χ_{sps} . The symmetry of the entire system requires that $\chi_{YYZ} = \chi_{XXZ}$ and $\chi_{YZY} = \chi_{XZX}$. (Thus, in the actual calculation of the susceptibility, χ_{YYZ} and χ_{XXZ} are averaged to give χ_{ssp} , and χ_{YZY} and χ_{XZX} to χ_{sps} .) In Eq. (2), the local field correction [27,31] at the surface is neglected, due to the lack of information on the dielectric properties of the surface; although the local field correction might affect the absolute intensity of SFG spectra, its frequency dependence can be considered insignificant for the interpretation of the SFG spectra.

To deal with the vibrational structure as a function of ω_{IR} , β is approximated solely by the IR resonant frequency term [36,41],

$$\beta_{pqr}(\omega_{\text{SFG}}, \omega_{\text{vis}}, \omega_{\text{IR}}) \approx \frac{\langle 0 | \hat{\alpha}_{pq} | v \rangle \langle v | \hat{\mu}_r | 0 \rangle}{\omega - \omega_{\text{IR}} - i\gamma}, \quad (3)$$

where $\hat{\alpha}$ and $\hat{\mu}$ are the molecular polarizability and dipole moment operators, respectively. $|0\rangle$ and $|v\rangle$ are the vibrational ground and excited eigenstates, whereas ω corresponds to the energy gap of $|v\rangle$ from the ground state $|0\rangle$. (Note that we adopt atomic units throughout.) The transition matrix elements in Eq. (3) are given as the derivatives by the vibrational mode under the harmonic oscillator assumption,

$$\langle v = 0 | \hat{A} | v = 1 \rangle \approx \sqrt{\frac{1}{2m\omega}} \left(\frac{\partial A}{\partial Q} \right), \quad (4)$$

$$A = \alpha_{pq} \text{ or } \mu_r,$$

where Q is the normal mode coordinate and m is the reduced mass of the mode. (The accuracy of Eq. (4) is satisfactory for the water O–H stretching vibration, as discussed in Section 2.3.1 and Table 2.) The damping factor γ in Eq. (3) could be in principle represented with the dephasing rate between $|v\rangle$ and $|0\rangle$ states [41], but is not generally available. We have roughly estimated it as twice an experimental estimate of the vibrational popula-

tion relaxation rate of OH stretching in water, $\gamma \approx 2 \times (3 \text{ ps})^{-1} = 22 \text{ cm}^{-1}$ [43]. (This estimate would be generally unreliable [44], but is sufficient for the case of water where T_1 is very short.) The approximate form of Eq. (3) adopted in this study is then

$$\beta_{pqr} \approx \frac{1}{2m\omega} \left(\frac{\partial \alpha_{pq}}{\partial Q} \right) \left(\frac{\partial \mu_r}{\partial Q} \right) \left[\frac{\omega - \omega_{\text{IR}}}{(\omega - \omega_{\text{IR}})^2 + \gamma^2} + \frac{i\gamma}{(\omega - \omega_{\text{IR}})^2 + \gamma^2} \right]. \quad (5)$$

In what follows, we assume that Eq. (5) has no explicit dependence of the visible frequency ω_{vis} , based on an assumption of small dispersion in the polarizability, since ω_{vis} is usually off-resonant and smaller than the electronic transition frequency. In order to check this assumption, we have carried out ab initio calculations at the Hartree–Fock (HF)/d-aug-cc-pVTZ [45] level to confirm that the frequency-dependent polarizability $\alpha(\tilde{\nu})$ of a water molecule, or its derivative by a local O–H distance $\partial\alpha(\tilde{\nu})/\partial r_1$, at $1/\tilde{\nu} = 532 \text{ nm}$, a typical experimental visible wavelength, is the same as the static counterpart to within 4%.

2.2. Vibrational mode character and OH frequency shift

A remaining task before applying Eq. (5) is to define the normal mode coordinate Q and vibrational energy level ω in the fluctuating condensed phase environment. Here, we focus on the normal modes of the water OH stretching band to compare with actual SFG experiments. In a simple two-state treatment of the water OH stretching without taking account of bending overtones [46], the vibrational eigenstate $|v\rangle$ of the OH stretching mode is represented by a linear combination of the two local OH stretching modes $|1\rangle, |2\rangle$ of a water molecule,

$$|v\rangle = C_1|1\rangle + C_2|2\rangle. \quad (6)$$

The derivatives in Eq. (5) are then conveniently expressed as

$$\frac{\partial A}{\partial Q} = C_1 \frac{\partial A}{\partial r_1} + C_2 \frac{\partial A}{\partial r_2}, \quad A = \alpha_{pq} \text{ or } \mu_r, \quad (7)$$

where r_1 and r_2 are the two intramolecular OH distances. The reduced mass m in Eq. (5) is taken as that of the local OH stretching because of the equal mass for the two local modes.

The coefficients (C_1, C_2) are determined via the two-state vibrational eigenequation,

$$\begin{bmatrix} \omega_1 - \omega & V_{12} \\ V_{12} & \omega_2 - \omega \end{bmatrix} \begin{bmatrix} C_1 \\ C_2 \end{bmatrix} = 0. \quad (8)$$

In the gas phase, where two local OH modes are equivalent ($\omega_1 = \omega_2$), the normal mode is either a purely symmetric stretching ($C_1/C_2 = +1$) or an antisymmetric stretching ($C_1/C_2 = -1$). The energy gap between the two eigenstates is 99 cm^{-1} , so that the coupling V_{12} is half of the energy gap, i.e. $V_{12} = 49.5 \text{ cm}^{-1}$. (The symmetric and antisymmetric OH stretching frequencies of H_2O are 3657 and 3756 cm^{-1} , respectively [47].) In liquid water, we will assume the coupling V_{12} to be the same, whereas the local OH frequencies ω_1, ω_2 are expected to suffer substantial red shifts due to the hydrogen-bonded environment, and the fluctuating environment can break the equivalence of the two local modes, $\omega_1 \neq \omega_2$.

It is well known experimentally that the OH stretching band is substantially red shifted, by as much as several hundred cm^{-1} , in water or ice due to hydrogen bonding [48–50]. The mechanism of the frequency shift is still not well established, and several models have been proposed [51–54]. Here, we seek a simple analytical model readily applicable in MD simulations and capable of fitting the frequency shifts obtained by a more rigorous ab initio treatment.

The potential energy of an isolated water molecule along a local OH stretch around the minimum point is expressed up to the third order in the one-dimensional displacement r ,

$$E = E_0 + \frac{1}{2}k_0r^2 + \frac{1}{6}l_0r^3. \quad (9)$$

We suppose that the local solvation environment is represented by a force F and its derivative G acting along the OH bond. The force F shifts the equilibrium position of the OH distance by $\Delta r = F/k_0$. This in turn changes the force constant at the

equilibrium position from k_0 to $k_0 + l\Delta r$ due to the bond anharmonicity. The force derivative G due to the interaction with the environment directly augments or reduces the potential curvature along the OH distance. The frequency shift is therefore given as

$$\Delta\omega = \sqrt{\frac{k_0 + l\Delta r + G}{m}} - \sqrt{\frac{k_0}{m}}, \quad (10a)$$

$$\Delta\omega \approx \sqrt{\frac{k_0}{m}} \left(\frac{lF}{2k_0^2} + \frac{G}{2k_0} \right), \quad (10b)$$

$$\Delta\omega \approx \sqrt{\frac{k_0}{m}} \left(\frac{lF}{2k_0^2} \right). \quad (10c)$$

The final expression (10c) involves two further approximations: (i) linearization of the square root and (ii) neglect of the G term compared to the F term. The former approximation holds very well up to frequency shifts of $500\text{--}600 \text{ cm}^{-1}$, and is sufficient in the present context. The latter approximation, which assumes that the effect of the internal bond anharmonicity is dominant over that of the interaction-induced anharmonicity, a common assumption in dephasing theory [44], will be justified in Section 2.3.2 via analysis of a model cluster system.¹ In the water context, the picture associated with Eq. (10c) is consistent with previous work by Reimers and Watts [53].

To implement Eq. (10c), the parameters k_0 and l are obtained via ab initio MO calculations described in Section 2.3, and the force F in the instantaneous environment is calculated in MD simulations, described in Section 3. Although the above model is a crude one, its performance is satisfactory as shown in the next section.

¹ Approximation (ii) differs from the conclusion of Rey and Hynes [55] in that the G term is significant in the frequency shift in the case of the CN^- vibration in water, but the effect of the G term in CN^- mainly comes from the repulsive force of ion solute–solvent interactions. The G term is not significant in the present system where the solvent interaction on the OH stretching is dominated by the electrostatic force, but little affected by the repulsive Lennard-Jones force between heavy atoms.

Finally, in the above discussion based on the two-state eigenequation (8), we neglected any delocalization of the vibrational modes among water molecules. This is a reasonable approximation in the high frequency region of O–H stretching, whereas collective vibrations in e.g. librational normal modes become substantial below 900 cm^{−1} [56].

2.3. *Ab initio* calculations of water molecular properties

To complete the preceding discussion, we will make use of *ab initio* MO methodology to calculate several properties of water molecules; (i) the force constant k_0 and anharmonicity l in Eqs. (9)–(10c), (ii) the dipole and polarizability derivatives $\partial A/\partial r$ in Eq. (7), (iii) the frequency shift (Eq. (10c)), and (iv) the influence of the environment on the coupling element V_{12} in Eq. (8) and $\partial A/\partial r$. All of the MO calculations described below were performed with **GAUSSIAN 98** [57].

2.3.1. Single water properties

The first two properties (i) and (ii) are calculated for a single H₂O in vacuum. The reference geometry of a H₂O is taken from the experimental equilibrium geometry [47]: $r(\text{OH}) = r_0 \equiv 0.9575 \text{ \AA}$, $\theta(\text{HOH}) = 104.51^\circ$, and the derivative was taken by 5-point numerical differentiation of different OH distances of one O–H bond with a displacement step of $\Delta = 0.05 \text{ \AA}$, i.e., $r(\text{OH}) = r_0$, $r_0 \pm \Delta$, $r_0 \pm 2\Delta$, while the other OH bond distance and the HOH angle are fixed. The *ab initio* method employed here is B3LYP [58,59]/d-aug-cc-pVTZ [45], which is sufficient for the calculation of polarizabilities [60].

For each of the five geometries, the dipole moment, polarizability and potential curvature along the local OH direction were calculated. The calculated dipole moment and isotropic polarizability are 1.85 D and 10.01 bohr³, respectively, which are consistent with the corresponding experimental values, 1.85 D and 9.92 bohr³ [47]. The results are summarized in Table 1, where the body-fixed *xyz* axes definition is taken such that the *z* axis points parallel to the local OH bond whose distance is varied, the *y* axis points normal to the

Table 1

Selected *ab initio* properties of a water molecule at the B3LYP/d-aug-cc-pVTZ level ($k_0 = 0.548$; $l = -1.991$)^a

$\partial\mu_r/\partial r_1$	$r = x$	$r = y$	$r = z$
	−0.058	0.000	0.157
$\partial\alpha_{pq}/\partial r_1$	$q = x$	$q = y$	$q = z$
$p = x$	1.539		
$p = y$	0.000	1.656	
$p = z$	−0.163	0.000	7.200

^a Force constant k_0 along a local OH bond, its derivative l with respect to the OH distance r_1 , dipole moment derivative $\partial\mu_r/\partial r_1$, and polarizability derivative $\partial\alpha_{pq}/\partial r_1$. See Fig. 1(a) for the definition of the body-fixed coordinates (units: a.u.).

molecular plane, and the other OH is on the positive side of the *x* axis (see Fig. 1(a)). Table 1 indicates that the *z* component of the dipole moment derivative $\partial\mu_z/\partial r_1$ is dominant, whereas the perpendicular *x* component $\partial\mu_x/\partial r_1$ is 1/3 of the *z* component, but not negligibly small. For the polarizability derivative $\partial\alpha/\partial r_1$, the *xx* and *yy* components are nearly identical and are about 1/4 of the *zz* component. These values are consistent with experimental estimates, $\alpha_{||}(\partial\alpha_{zz}/\partial r_1) = 7.07 \text{ a.u.}$, $\alpha_{\perp}(\partial\alpha_{xx}/\partial r_1 = \partial\alpha_{yy}/\partial r_1) = 2.26 \text{ a.u.}$ [61], which have been utilized to interpret the Raman spectra of water OH stretching band intensity, considering that the Raman intensity is less sensitive to the environment than the IR intensity [62,63].²

The assumption (4) is now examined via the same level of *ab initio* calculations. The potential energy curve, dipole moment and polarizability of a H₂O were calculated with a varying O–H₁ distance from $r(\text{O–H}_1) = r_0 - 3\Delta$ to $r_0 + 6\Delta$ ($r_0 = 0.9575 \text{ \AA}$, $\Delta = 0.05 \text{ \AA}$) with the other OH bond distance and the HOH angle fixed. Then the quantum energy levels and vibrational wave functions of the ground $v = 0$ and first excited

² Here we note that the perpendicular components of the polarizability derivative ($\partial\alpha_{xx}/\partial r_1$, $\partial\alpha_{yy}/\partial r_1$) are quite sensitive to the accuracy of the wave function. For example, when the HF/6-311 + G(d, p) wave function is used, the diagonal elements of $\partial\alpha/\partial r_1$ turn to be 0.555(*xx*), 0.100(*yy*), 7.664(*zz*). The HF/d-aug-cc-pVTZ values are instead 1.354(*xx*), 1.297(*yy*), 7.290(*zz*), which are closer to the values in Table 1. The significant underestimate of the perpendicular components is to be attributed mainly to the insufficient basis set rather than the electron correlation [60].

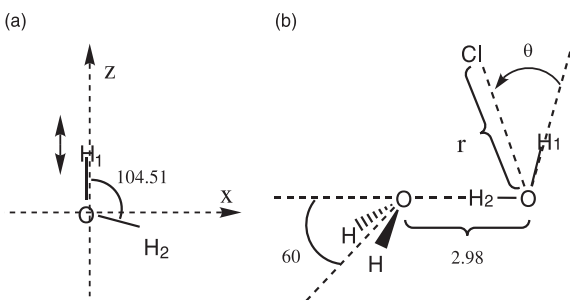


Fig. 1. Schematic pictures to define spatial coordinates and molecular geometries: (a) definition of the body-fixed xyz frame of a water molecule, (b) definition of the varying coordination geometry in the $\text{Cl}^-(\text{H}_2\text{O})_2$ cluster. Units: distances in Å, angles in degree.

$v = 1$ vibrational states were obtained from the one-dimensional potential energy curve by diagonalizing the Hamiltonian matrix of the discrete variable representation, and the transition frequency ω from $v = 0$ to $v = 1$ was obtained. The matrix elements $\langle v = 0 | \hat{A} | v = 1 \rangle$ of the left hand side of Eq. (4) were calculated by numerical integration. The derivative $\partial A / \partial r_1$ was calculated by the five-point numerical differentiation around the equilibrium O–H₁ bond length $r(\text{O–H}_1) = r_0$. The results of the comparison are given in Table 2, which shows that Eq. (4) is accurate to within 1–6% for the dipole moment and polarizability.

2.3.2. Perturbation by hydrogen bonding

We next turn to the perturbation by hydrogen bonding for the water properties and examine in detail the model treatment of the OH frequency shifts given in Section 2.2. For this purpose, we

Table 2
Examination of Eq. (4) by comparing the left-hand side (LHS, $\langle v = 0 | \hat{A} | v = 1 \rangle$) with the right-hand side (RHS, $\sqrt{1/2m\omega}(\partial A / \partial r_1)$) for the water O–H stretching^a

A	LHS	RHS	Ratio (R/L)
μ_x	−0.00721	−0.00763	1.058
μ_z	0.01947	0.02043	1.049
α_{xx}	0.20200	0.20450	1.012
α_{yy}	0.21331	0.21756	1.020
α_{zz}	0.99904	0.95787	0.959

^a See Fig. 1(a) for the definition of the body-fixed coordinates. Units: a.u.

will use a $\text{Cl}^-(\text{H}_2\text{O})_2$ cluster in ab initio MO calculations as a model system of hydrogen bonding. This choice is motivated by the fact that chlorine–water clusters have been extensively studied both spectroscopically [64,65] and theoretically [66–69] as a model of hydrogen bonding, and allows the examination of large frequency shifts comparable to those observed in liquid water. In particular, the stable coordination of a chlorine anion to a water molecule causes a OH frequency red shift of as much as 560 cm^{-1} [64], which is comparable to the amount of actual OH frequency shift in water or ice [48–50]. The frequency red shift of the hydrogen-bonded OH in the water dimer is, in comparison, only about 100 cm^{-1} [70].

The geometry of the $\text{Cl}^-(\text{H}_2\text{O})$ cluster is shown in Fig. 1(b), where the geometry of the constituent water dimer is taken from experiment [71]. H₁ is coordinated to Cl[−] at varying positions, whereas H₂ is hydrogen-bonded to the second water molecule. The Cl–O distance and the Cl–O–H₁ angle are taken as $R(\text{Cl–O}) = 3.2, 3.7, 4.2 \text{ \AA}$ and $\theta(\text{Cl–O–H}_1) = -90^\circ, -60^\circ, -30^\circ, 0^\circ, 30^\circ, 60^\circ$, so that a total of 18 geometries of Cl[−] coordination are considered with C_s symmetry. The bare water dimer is taken as the reference. The second water molecule has been introduced both to “pin” the O–H₂ bond of the first water and to give the OH vibration of the first water some local-mode character, since in the actual condensed environment the OH modes are fairly localized, as will be discussed in Section 4. For each position of Cl[−], the O–H₁ bond stretching frequency shift is estimated in two ways, via the model described in Section 2.2 and ab initio.

In the model treatment of Section 2.2, the force along the O–H₁ direction is evaluated by the site–site electrostatic interaction. The charge at the Cl[−] site is -1 , and the partial charges at water sites are taken from the SPC/E model [72] ($q_O = -0.8476$, $q_H = 0.4238$), which will be used in Sections 3 and 4. For purposes of comparison, we also examined the SPC/G water model [73], where the partial charges are scaled to fit the gas-phase dipole moment ($q_O = -0.6572$, $q_H = 0.3286$).

In the ab initio treatment, the MP2/6-31++G(d,p) [57] level was utilized for the calcu-

lation of the potential energy surface. At each Cl^- position, the one-dimensional potential energy curve is obtained along the $\text{O}-\text{H}_1$ distance from $r_0 - 3\Delta$ to $r_0 + 6\Delta$ with other atoms fixed. Then, by numerically calculating the quantum energy levels of the ground $v = 0$ and first excited $v = 1$ vibrational states as described in Section 2.3.1, the transition frequency from $v = 0$ to $v = 1$ is obtained. This ab initio calculation takes into account the anharmonicity along the local $\text{O}-\text{H}$ distance, which has been shown to be quite important for the frequency shift [74].

The comparison of these two methods for calculating the frequency shift due to the hydrogen bond of Cl^- is displayed in Fig. 2, which indicates a good correlation between the two treatments. Particularly, the present model can correctly distinguish between linear and perpendicular coordinations to the OH bonds, which we regard as an advantage over other possible model treatments of hydrogen bonding, such as that based on just the

energetics or on the nearest neighbor distance. When the Cl^- approaches the hydrogen of the OH collinearly ($\angle \text{O}-\text{H} \cdots \text{Cl}^- \approx 180^\circ$), a strong hydrogen bond is formed, leading to a large red shift; when the $\text{O}-\text{H} \cdots \text{Cl}^-$ angle is $\sim 90^\circ$, a small frequency shift results, even if the $\text{Cl}^- \cdots \text{H}$ distance is fairly small.

Fig. 2(a) compares the model treatment of Eq. (10b) with that of Eq. (10c), and indicates that the interaction force derivative G of Eq. (10b) has generally much less influence than does the interaction force F and thus may be neglected. Accordingly, we will use Eq. (10c) in our subsequent analysis. Fig. 2(a) also shows that the model treatment somewhat *overestimates* the OH frequency shifts. This feature is to be partly attributed to the SPC/E water model, which involves enhanced polarity appropriate for condensed-phase water. Although the enhanced polarity is justified in the bulk or surface region of water [28], it should not be valid for the isolated small cluster.

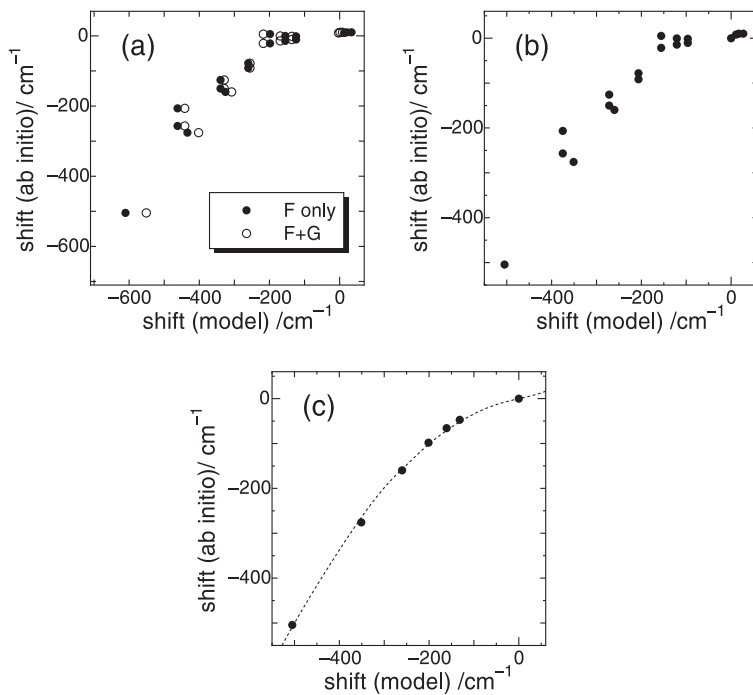


Fig. 2. Comparison of the OH frequency shifts by the model of Section 2.2 and ab initio treatments. (a) SPC/E and (b,c) SPC/G water models are used in the model treatment. The black circles in (a)–(c) correspond to Eq. (10c), whereas the white circles in (a) correspond to Eq. (10b). The dotted line in (c) shows the calibration line equation (11).

The correlation is improved when the SPC/G water model is used (Fig. 2(b)). Fig. 2(b), however, still displays some discrepancy, particularly in the small red shift frequency region. Thus, we calibrate the frequency shift in order to further improve the model prediction. The calibration line is determined via least square fitting of the ab initio calculations of the linear Cl^- – H_1 – O coordination with a varying Cl^- – O distance (3.2–5.7 Å). The fitted result is

$$|\Delta\tilde{v}| = 0.1762 |\Delta\tilde{v}_{\text{model}}| + 1.647 \times 10^{-3} |\Delta\tilde{v}_{\text{model}}|^2, \quad (11)$$

whose performance is shown in Fig. 2(c). The OH frequency shifts will be estimated from the MD results with Eq. (11), with the origin of the local OH frequency taken to be 3707 cm^{-1} , i.e. an average of symmetric and antisymmetric stretching frequencies of water in the gas phase.

We next consider the coupling V_{12} in Eq. (8) between the two local O–H stretching modes and the influence of the hydrogen bonding on them. As noted in Section 2.2, we assume that the coupling V_{12} is constant. While this is consistent with the treatment of Refs. [53,74], it disagrees with Refs. [51,52] which argues that the off-diagonal coupling of the harmonic force constant is sensitive to the hydrogen bonding and even changes its sign. To examine this issue, we calculated at the MP2/6-31++G(d,p) level the off-diagonal element k_{12} of the harmonic force constant between the two local O–H stretching modes for the $\text{Cl}^- \cdot (\text{H}_2\text{O})_2$ cluster. The results of k_{12} are shown in Fig. 3. If we

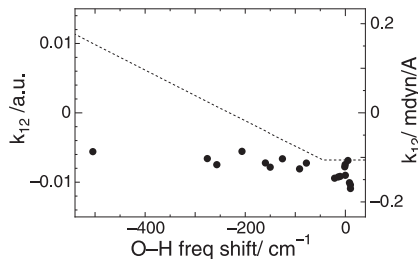


Fig. 3. Off-diagonal element k_{12} of the harmonic force constant of water as a function of the OH frequency shift. The dotted line corresponds to Eq. (4) of Ref. [51].

assume, just for this purpose, the two-dimensional harmonic potential of intramolecular vibration

$$E_{\text{harmonic}} = \frac{1}{2}k_1\Delta r_1^2 + \frac{1}{2}k_2\Delta r_2^2 + k_{12}\Delta r_1\Delta r_2, \quad (12)$$

where Δr_1 and Δr_2 are the displacements of the two local O–H stretches, the coupling V_{12} would be proportional to k_{12} as

$$V_{12} = \frac{k_{12}}{2\sqrt{m(k_1k_2)^{1/2}}}. \quad (13)$$

The ab initio results of Fig. 3 indicate a less drastic influence by the hydrogen bonding on k_{12} than previously thought, and allow us to take a constant V_{12} as a useful working approximation. (In a more quantitative sense, however, Eq. (12) or Eq. (13) is not a very good approximation since the vibrational anharmonicity is neglected. The calculated result of $k_{12} \sim -0.01$ a.u. in Fig. 3 without the chlorine perturbation leads to $V_{12} \approx 36 \text{ cm}^{-1}$, which underestimates the value 49.5 cm^{-1} estimated from the experimental energy gap between the symmetric and antisymmetric stretching states by 30%. In our subsequent analysis, the experimental value of V_{12} will be employed which effectively includes both the harmonic and anharmonic components of the coupling.)

The $\text{Cl}^- \cdot (\text{H}_2\text{O})_2$ cluster is also utilized to assess the perturbation by hydrogen bonding on the derivatives $\partial A / \partial r_1$ in Eq. (4), where $A = \alpha_{pq}$ or μ_r , which are crucial for Raman and IR intensities, respectively [75]. For each Cl^- position described above, the dipole moment and polarizability of the entire cluster were calculated with a varying O–H₁ distance, $r(\text{O–H}_1) = r_0 \pm 2\Delta$, $r_0 \pm \Delta$, r_0 , and the derivative was taken via five-point numerical differentiation. The wave functions we employed here are B3LYP with d-aug-cc-pVDZ for the oxygen atom of the central water, aug-cc-pVDZ for the hydrogen atoms H₁ and H₂ of the central water and Cl[−], and 6-31+G(d,p) for the second water. In this treatment, the central oxygen has two sets of diffuse basis functions, while the other atoms are augmented with a single set of diffuse functions (too many diffuse basis functions in the same spatial region of the cluster would be redundant).

The results for $\partial\mu / \partial r_1$ and $\partial\alpha / \partial r_1$ are displayed in Fig. 4 as a function of the OH frequency shift.

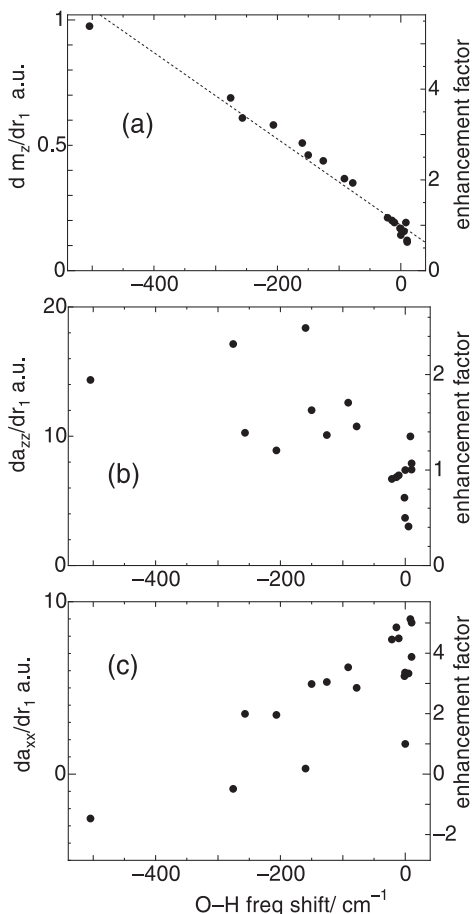


Fig. 4. Hydrogen-bonding perturbation on dipole and polarizability derivatives expressed as a function of the OH frequency shift: (a) $\partial\mu_z/\partial r_1$, (b) $\partial\alpha_{zz}/\partial r_1$, (c) $\partial\alpha_{xx}/\partial r_1$. The right axes show the enhancement factor compared to the gas-phase values. The dotted line in (a) indicates the linear correlation obtained by least square fitting.

Fig. 4(a) portrays a good linear correlation between the OH frequency shift $\Delta\tilde{\nu}$ and the enhancement of $(\partial\mu_z/\partial r_1)/(\partial\mu_z/\partial r_1)_0$ as

$$\frac{\partial\mu_z/\partial r_1}{(\partial\mu_z/\partial r_1)_0} = 1.0 - 9.5138 \times 10^{-3} \Delta\tilde{\nu}, \quad \Delta\tilde{\nu}/\text{cm}^{-1}, \quad (14)$$

where the subscript 0 in the denominator indicates the dipole derivative evaluated with no perturbation by Cl^- . It is well known that the IR intensity of the OH stretching band is significantly

enhanced by hydrogen bond formation [76,77], and since the IR intensity is proportional to the square of the dipole moment derivative, Eq. (14) correctly predicts this trend. For example, $\Delta\tilde{\nu} = -300 \text{ cm}^{-1}$ would lead to an IR enhancement factor of $(3.85)^2 = 14.9$. On the other hand, as seen in Fig. 4(b) and (c), the polarizability derivative does not show any clear correlation with the OH frequency shifts. The perturbation on the main component of the polarizability derivative, $\partial\alpha_{zz}/\partial r_1$ (Fig. 4(b)), is less crucial than that of the dipole derivative, $\partial\mu_z/\partial r_1$ (Fig. 4(a)), and it does not necessarily bring about an enhancement to the polarizability derivative. The perpendicular component $\partial\alpha_{xx}/\partial r_1$ shows more significant variation in Fig. 4(c) than does the parallel component, although this minor component is of less importance to the overall susceptibility. The Raman intensity is generally less sensitive to the environment, and thus readily transferable, while IR intensity is generally quite sensitive to the environment [62,63]. This assumption might break down either when the Raman transition is close to a resonance, or when the upper electronic structure of a Raman transition is of a charge transfer character and is significantly affected by the environment. However, in the present system of pure water with the off-resonant condition, the Raman intensity is expected to be less sensitive to the environment, as shown in Fig. 4(b) and (c). Therefore, in the following discussion, we neglect the perturbation effect on the polarizability derivative by hydrogen bonding. (A more rigorous treatment would be required for a quantitative simulation.) When calculating $\partial\mu_z/\partial Q$ in MD simulations using Eq. (7), the $\partial\mu_z/\partial r_{1,2}$ components of each water molecule are enhanced from the gas-phase value of Table 1 by a factor given by Eq. (14), in order to incorporate the solvent perturbation on the SFG intensity.

3. MD simulations

MD simulations were performed on an infinite film geometry of water with two-dimensional

periodic boundary conditions. A periodic cell contains $N=432$ water molecules with a periodic length of 18.64 Å for the X, Y directions orthogonal to the perpendicular direction Z , so that the film is constructed by approximately 12 vertical layers. Microcanonical MD calculations were performed, and the time integration was carried out by the velocity Verlet algorithm [78] with the time step of 2 fs. The temperature was maintained at 273.15 K by simply scaling the particle velocities. During the initial stage of equilibration, a periodic boundary condition along the Z direction was also imposed on the system with a vertical periodic length of 37.29 Å, so that the system has a constant density of 0.997 g/cm³ under the full (three-dimensional) periodic boundary conditions. After this initial equilibration stage of 100 ps duration, the vertical periodic boundary condition was removed and a further equilibration run was carried out for 100 ps before the sampling run for 100 ps. The configuration was sampled every 0.1 ps during the sampling run. Eight independent trajectories were generated with different initial configurations, and the results were statistically averaged. The total time of sampling was 800 ps.

The water model employed for the MD simulation portion of the present work is SPC/E [72], which has been demonstrated in previous MD work to give reasonable surface structure for water [30,31]. During the initial equilibration stage with three-dimensional periodic boundary conditions, the molecular interactions were simply cut off at the center-of-mass distance of half of each periodic length. During the subsequent simulations with two-dimensional periodic boundary conditions, interactions beyond the lateral cutoff length were incorporated via the dielectric continuum treatment originally proposed by Torrie and Valleau [79] and subsequently validated [28,80].

The result for the vertical density profile is shown in Fig. 5, where the simulation data are least square fitted with a hyperbolic tangent function [23,24,27,30],

$$\rho(Z) = a \{1.0 - \tanh[b(Z - c)]\}, \quad \rho(Z)/\text{g/cm}^3, \quad Z/\text{\AA},$$

$$a = 0.491, \quad b = 0.567, \quad c = 18.83. \quad (15)$$

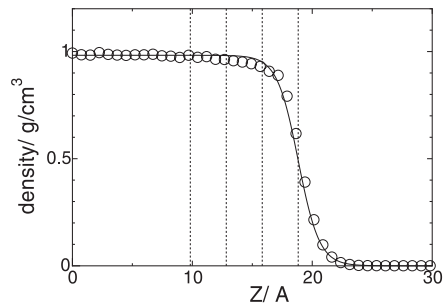


Fig. 5. Density profile as a function of vertical depth Z , where $Z = 0$ denotes the center of the film. The open circles correspond to the simulation data and the solid line is the result of least square fitting. The dotted vertical lines at $Z = Z_{\text{Gib}} (= 18.83 \text{ \AA})$, $Z_{\text{Gib}} - 3 \text{ \AA}$, $Z_{\text{Gib}} - 6 \text{ \AA}$, $Z_{\text{Gib}} - 9 \text{ \AA}$ define a segmentation inside the Gibbs dividing surface with 3 Å spacing.

The Gibbs dividing surface is located at $Z_{\text{Gib}} = c = 18.83 \text{ \AA}$, and the bulk density and the 10–90 thickness of the surface are $2a = 0.973 \text{ g/cm}^3$ and $2.1972/b = 3.88 \text{ \AA}$, respectively. The vapor density is assumed to be negligible. Fig. 5 gives a segmentation below the Gibbs dividing surface with a 3 Å spacing for the purpose of later analysis; the 3 Å spacing nearly corresponds to the size of a water molecule so that we will consider the spatial region $Z > Z_{\text{Gib}} - 3 \text{ \AA}$ to be the surface top monolayer.

The surface thickness is comparable to some previous simulation results [23,24,27,29], but is somewhat larger than previous simulations with the SPC/E model [30,31], which used different treatment of long-range forces. It has been pointed out [31] that the surface thickness is a rather sensitive quantity to the intermolecular potential and treatment of long-range correction. On the other hand, the experimental data on surface thickness show significant discrepancy: 7.1 Å at 0–20°C by ellipticity [81] and 3.2–3.3 Å at 25°C by X-ray [82,83]. The significantly larger experimental value obtained by the ellipticity measurements compared to those of the simulations has been attributed to the effect of long-wavelength capillary waves, excluded by finite size periodic boundary conditions [27,30,31]. This should not, however, be a serious concern in the present work since, as we will argue in Section 4, the SFG signal is dominated by the top monolayer of the surface.

4. Analysis of the SFG spectrum

4.1. Simulated SFG spectrum

The SFG spectrum of water is simulated using the results of Section 2 and the MD results of Section 3. Fig. 6 shows the simulated *ssp* polarization SFG spectrum. In this analysis, the nonresonant component of the susceptibility χ_{ssp}^{nr} is assumed to be constant (-0.1 a.u., cf. Fig. 7). χ^{nr} is the only parameter besides γ of Eq. (5) not derived from ab initio calculations or MD simulations, and has been determined to give a proper magnitude of a dip to the spectrum at ~ 3600 cm^{-1} . (The resulting relative amplitude of the nonresonant component compared to the resonant one is reasonably consistent with an experimental suggestion by Shen and co-workers [42].) Fig. 6 captures the essential features of the experimental SFG spectrum [38,42] quite well. The spectrum exhibits two peaks, a broad one at about 3000 – 3500 cm^{-1} and a sharp one peaked at ~ 3700 cm^{-1} , with a distinct dip between the two. The former band has been usually assigned to the stretching vibration of hydrogen-bonded OH moieties while the latter has been assigned to the dangling OH stretch [38,42].

4.2. Surface susceptibility: *ssp* versus *sps*

The SFG spectrum can be further analyzed by investigating the susceptibility χ , which involves both amplitude and phase (or sign). Fig. 7 shows

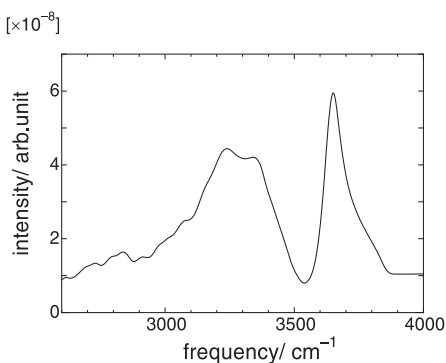


Fig. 6. Simulated SFG spectrum of water of *ssp* polarization. The fixed visible wavelength is 532 nm.

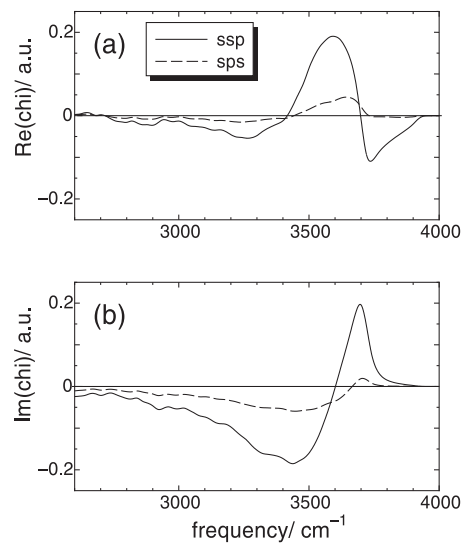


Fig. 7. Resonant susceptibility χ^r per unit surface area of *ssp* (—) and *sps* (---) polarization combinations as a function of frequency. The panels (a) and (b) show the real and imaginary parts, respectively.

the spectra of the resonant susceptibility χ^r and compares the *ssp* and *sps* polarization combinations, the former being the focus of all previous experimental studies. The calculated amplitude of the latter *sps* combination, χ_{sps}^r , is quite small over the entire frequency region considered, less than $1/3$ of the amplitude of the *ssp* combination, χ_{ssp}^r . This is consistent with a previous experimental suggestion derived by comparing *ssp* and *sps* intensities (Eq. (5) of Ref. [42]). We do not give the SFG spectrum of the *sps* combination, since the nonresonant component of *sps* combination χ_{sps}^{nr} is not available. The comparison of χ_{ssp}^r and χ_{sps}^r in Fig. 7 is consistent with the experimental result [42] that the intensity of the *sps* spectrum, which is proportional to $|\chi_{sps}|^2$, is less than 10% of the *ssp* intensity. Fig. 7 also reveals that the *sps* amplitude in the dangling bond region ~ 3700 cm^{-1} is more suppressed than at the hydrogen-bonded frequency range, 3000 – 3500 cm^{-1} . This implies, even within the small *sps* combination where the IR polarization is parallel to the surface, that the dangling OH signal is not well detected. Thus, in the following, we will deal exclusively with the *ssp* spectrum.

4.3. SFG surface specificity

It is widely accepted that SFG is surface specific when the bulk is isotropic, but it has not been clear how specific, i.e. involving only the first monolayer, a few top monolayers, or more. In order to assess the surface sensitivity in the present system, we have generated some virtual surface susceptibilities with an assumption that the contributions to the susceptibility would be restricted from the surface by varying the depth to examine the convergence behavior. A series of susceptibilities is given in Fig. 8, where the intermediate lines are based on the segmentation shown in Fig. 5. We see that 90% of the amplitude comes from the first two monolayers below the Gibbs dividing surface (the region $Z > Z_{\text{Gib}} - 6 \text{ \AA}$) in the hydrogen-bonded band ($< 3600 \text{ cm}^{-1}$) and from the first monolayer below the Gibbs surface ($Z > Z_{\text{Gib}} - 3 \text{ \AA}$) in the dangling bond band ($> 3600 \text{ cm}^{-1}$). The dangling bond band is somewhat more sensitive to the surface than the hydrogen-bonded band, and it exclusively detects the top monolayer. Even the hydrogen-bonded band is virtually dominated by

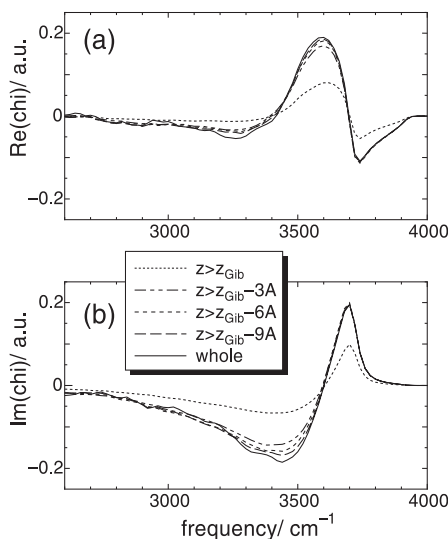


Fig. 8. Surface sensitivity of the susceptibility $\chi_{\text{ssp}}^{\text{r}}$ per unit surface area of water. The solid lines denote the whole susceptibility, and the other lines correspond to virtual susceptibilities within restricted systems by various depths from the surface to examine the convergence. (a) and (b) show the real and imaginary parts respectively. Unit: a.u.

the top monolayer and sensitive to only a few top monolayers.³ We also note in Fig. 8 that the vapor side of the surface outside the Gibbs dividing surface ($Z > Z_{\text{Gib}}$) gives a relatively minor contribution to the overall SFG intensity, a feature which can be attributed to its low density.

4.4. OH orientation at the surface

Fig. 7(b) or 8(b) exhibits opposite signs in the imaginary part of the *ssp* susceptibility $\chi_{\text{ssp}}^{\text{r}}$ ($\text{Im}(\chi_{\text{ssp}}^{\text{r}})$) in the hydrogen-bonded band ($\lesssim 3600 \text{ cm}^{-1}$) and in the dangling bond band ($\gtrsim 3600 \text{ cm}^{-1}$). This feature carries structural information about the surface, as discussed below. The molecular hyperpolarizability β , Eq. (5), has a Lorentzian ω_{IR} dependence, i.e. the real part of hyperpolarizability β changes its sign at $\omega_{\text{IR}} = \omega$ (the $|0\rangle \rightarrow |v\rangle$ resonance frequency), while the imaginary part of β retains its sign. Therefore, the opposite signs of $\text{Im}(\chi_{\text{ssp}}^{\text{r}})$ evidence opposite molecular orientation with respect to the surface normal. Table 1 and Eq. (5) indicate that a local O-H₁ stretching along the z axis of the body-fixed frame (cf. Fig. 1(a)) would induce positive prefactors of β_{xxz} and β_{yyz} in the same body-fixed frame. Thus, a local OH stretching mode pointing outwards to the vapor would contribute to positive $\text{Im}(\chi_{\text{ssp}}^{\text{r}})$, and one pointing inwards to the bulk to negative $\text{Im}(\chi_{\text{ssp}}^{\text{r}})$. This picture is supported by the distribution of the direction cosines of OH ($\cos \theta(\text{OH})$) at the surface in Fig. 9. Fig. 9(a) portrays an enhanced distribution of OH pointing towards the vapor, $\cos \theta(\text{OH}) \sim 1$, in the frequency region of the dangling bond band $> 3600 \text{ cm}^{-1}$, and a substantially reduced distribution around

³ These results of surface sensitivity are obtained in the case of pure water, but we note that the surface sensitivity might depend on the system composition, particularly when ions are involved. For example, dilute ionic solutions significantly enhance the SFG intensity of the hydrogen-bonded band [38–40,86,87], and this enhancement has been attributed to induced electric double layers by the ions, which bring about net orientational polarization of water in a large scale near the surfaces. In those cases, the hydrogen bond signal may be sensitive to deeper layers.

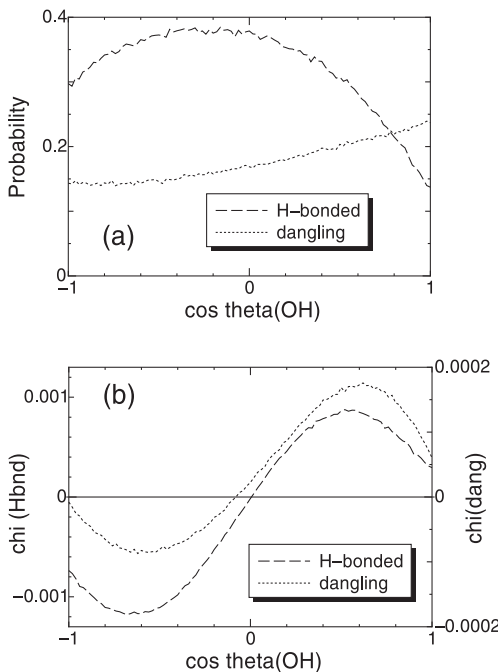


Fig. 9. (a) Distribution of the direction cosine from the surface normal of OH moieties in the first monolayer of the surface ($Z > Z_{\text{Gib}} - 3 \text{ \AA}$, Z is the coordinate of the center of mass). The number of OHs in each normal mode was counted with a weight of the squared local vibrational amplitude, $|C_1|^2$ or $|C_2|^2$. The dashed and dotted lines denote the distributions within the hydrogen-bonded band ($< 3600 \text{ cm}^{-1}$) and dangling bond band ($> 3600 \text{ cm}^{-1}$), respectively. The integrated probability density of both bands is normalized to unity. (b) Distribution of the frequency-averaged prefactor of the *ssp* susceptibility χ_{ssp}^r ($= (1/2m\omega)(\partial\alpha_{pq}/\partial Q)(\partial\mu_r/\partial Q)$ see Section 4). Units: a.u. per bohr² and unit angular volume ($\cos\theta(\text{OH})$). The left ordinate refers to the hydrogen-bonded frequency region, and the right ordinate to the dangling bond region.

$\cos\theta(\text{OH}) \sim 1$ in the hydrogen-bonded band frequency region $< 3600 \text{ cm}^{-1}$.

The relation between the surface susceptibility and the OH direction is highlighted in Fig. 9(b) via decomposition of the surface susceptibility on the OH direction cosine. The focus here is to abstract qualitative features and differences between the dangling bond frequency region ($> 3600 \text{ cm}^{-1}$) and the hydrogen-bonded region ($< 3600 \text{ cm}^{-1}$). In order to deal with the susceptibility separately in the two frequency regions, we need to define an averaged susceptibility in each frequency region. Since the molecular hyperpolarizability β_{pqr} of

Eq. (3) varies with the frequency ω_{IR} , the frequency-averaged susceptibility in either dangling bond or hydrogen-bonded region requires integration of β on the relevant frequency region. However, a simpler procedure can be followed. If the integration of β is carried out on the whole frequency domain instead of each frequency range, the result is in a simple analytical form and proportional to the prefactor of Eq. (3):

$$\int \beta_{pqr} d\omega_{\text{IR}} = \int \frac{\langle 0|\hat{\alpha}_{pq}|v\rangle\langle v|\hat{\mu}_r|0\rangle}{\omega - \omega_{\text{IR}} - i\gamma} d\omega_{\text{IR}} \\ = -i\pi \langle 0|\hat{\alpha}_{pq}|v\rangle\langle v|\hat{\mu}_r|0\rangle. \quad (16)$$

Therefore, the integration of β in the frequency region can be approximately circumvented. In the present analysis, just the prefactor $\langle 0|\hat{\alpha}_{pq}|v\rangle \times \langle v|\hat{\mu}_r|0\rangle = (1/2m\omega)(\partial\alpha_{pq}/\partial Q)(\partial\mu_r/\partial Q)$ was statistically averaged according to the resonance frequency ω in each frequency region.

The results in Fig. 9(b) are sinusoidal curves in both the frequency regions. A basic common feature is that the OH bonds with positive direction cosines contribute positively to the susceptibility, while those with negative direction cosines contribute negatively, which is understandable from the discussion on the water orientation in the preceding paragraph. However, the significant asymmetry of the direction cosine distribution (Fig. 9(a)) results in the net positive susceptibility in the dangling bond frequency region and the net negative susceptibility region in the hydrogen-bonded frequency region, respectively.

4.5. Dangling bond ratio

The dangling OH bond ratio at the surface is a convenient index to characterize the surface structure, and here we estimate it in terms of the SFG signal. A rough way of estimation would be based on the population ratio between the OH bonds in the dangling bond frequency region ($> 3600 \text{ cm}^{-1}$) and those in the hydrogen-bonded frequency region ($< 3600 \text{ cm}^{-1}$), which can be estimated as 35%:65% by integrating the distribution over $\cos\theta(\text{OH})$ in Fig. 9(a). This ratio, however, should overestimate the number of the surface dangling bonds, since all OH bonds having the

frequencies above 3600 cm^{-1} at the surface top monolayer have been counted as dangling, but Fig. 9(a) implies that a considerable portion of the “dangling” OHs point inwards toward the bulk. (The above ratio is appropriately higher than a previous experimental estimate $\sim 20\%$, which has been considered as a lower bound [42].) Therefore, in connection with the SFG dangling bond signal, here we regard the surface OH bonds contributing positively to the susceptibility in the frequency range above 3600 cm^{-1} as dangling. If we adopt this definition, Fig. 9(b) implies that the dangling bonds exist for $\cos\theta(\text{OH}) > -0.08$, and consequently the dangling bond ratio is estimated from Fig. 9(a) to be 21% in the overall surface OH moieties. This is consistent with the previous experimental suggestion mentioned above.

4.6. H_2O orientation at the surface

The above discussion on molecular orientation is based on the picture of the local OH stretching

direction. Alternatively, we can analyze the orientations of the water molecules themselves. The purpose of this analysis is to characterize the surface molecular orientation in the two different frequency bands, relevant to the SFG signal or the surface susceptibility. Fig. 10 gives the two-dimensional (θ, ϕ) distribution of the surface molecular orientation and Fig. 11, the two-dimensional decomposition of the *ssp* susceptibility. The definition of θ and ϕ is given in Fig. 10(c); θ is the angle between the surface normal and the dipole moment, and ϕ is the dihedral angle between the molecular plane and the plane defined by the surface normal and the dipole direction. Figs. 10 and 11 are the counterparts of Fig. 9(a) and (b), respectively.

Fig. 10(a) and (b) indicates that the molecular orientation of the surface water does not exhibit any remarkable difference between the different frequency regions. In both frequency regions, θ shows an approximate bell-shape distribution around $\theta \sim 90^\circ$, which implies that the dipole di-

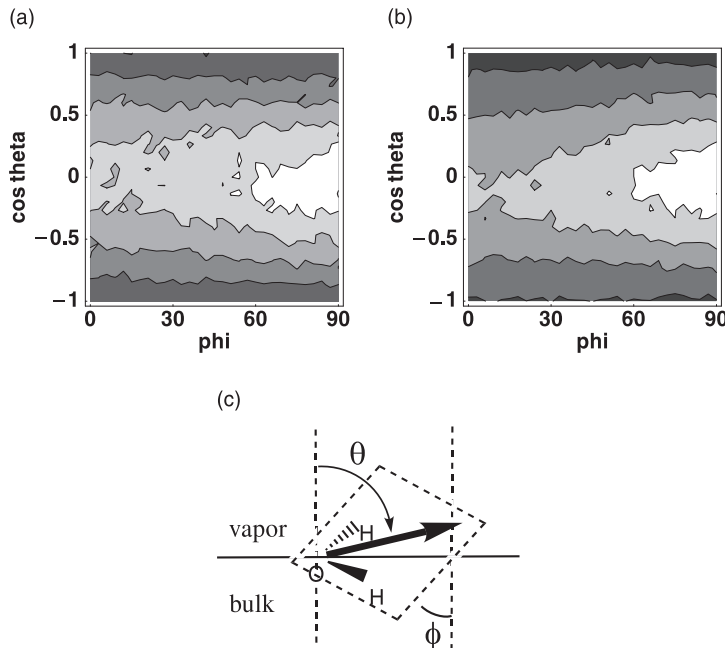


Fig. 10. Two-dimensional (θ, ϕ) distribution of molecular orientation in the surface top monolayer. (a) dangling bond region ($>3600\text{ cm}^{-1}$) and (b) hydrogen-bonded region ($<3600\text{ cm}^{-1}$). Units: ϕ/degree , contour/number density per bohr^2 and unit angular volume ($\cos\theta\phi$). In (a), the contour line bounding the lightest region is 10^{-2} and the contour spacing is 2×10^{-3} . In (b), the contour line bounding the lightest region is 2×10^{-2} and the contour spacing is 5×10^{-3} , (c) depicts the definition of θ and ϕ .

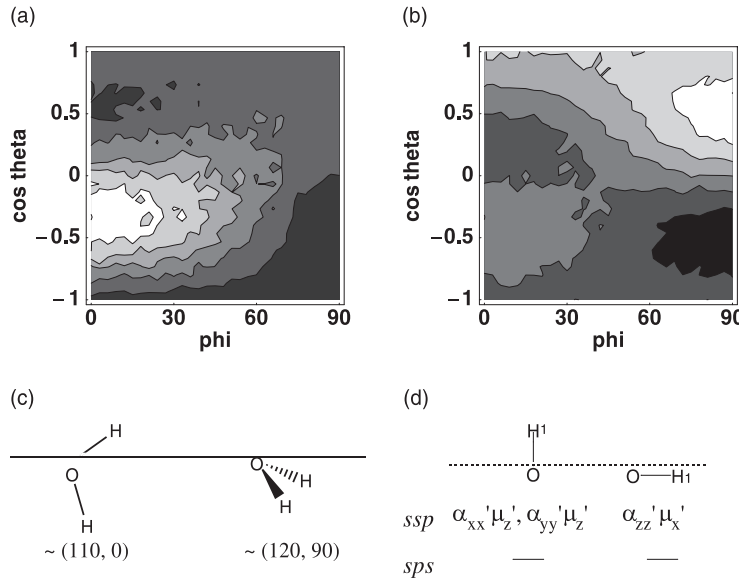


Fig. 11. Two-dimensional (θ, ϕ) decomposition of the frequency-averaged prefactor of the ssp susceptibility χ_{ssp}^r . (a) dangling bond region ($>3600 \text{ cm}^{-1}$) and (b) hydrogen-bonded region ($<3600 \text{ cm}^{-1}$). Units: ϕ/degree , contour/a.u. per bohr^2 and unit angular volume ($\cos \theta \phi$). In (a), the contour line bounding the lightest regions is 4×10^{-5} and the contour spacing is 10^{-5} . In (b), the contour line bounding the lightest region is 2×10^{-4} and the spacing is 10^{-4} . (c) shows a typical orientation in each frequency region represented with (θ, ϕ) . (d) Two schematic pictures of the surface OH bond with important components for the ssp/sps susceptibility in their body-fixed frame (Section 4).

rection tends to be parallel to the surface plane. Nevertheless, each OH direction has a fairly random distribution since the ϕ distribution is very broad with a maximum $\sim 90^\circ$. On the other hand, the decomposed ssp susceptibility on the (θ, ϕ) plane is noticeably different, as seen in Fig. 11(a) and (b). In the dangling bond frequency region of Fig. 11(a), the most substantial contribution comes from the orientation about $\theta \sim 110^\circ$ ($\cos \theta \sim -0.34$) and $\phi \sim 0^\circ$. Such an orientation at the surface typically gives a dangling OH toward the vapor (Fig. 11(c)), but is considerably tilted from the surface normal. This typical molecular orientation is also consistent with Fig. 9(b), which shows a positive peak at $\cos \theta(\text{OH}) \sim 0.6$. (Note the difference between θ and $\theta(\text{OH})$.) This insight on the dangling OH direction differs from a previous suggestion in Ref. [42] that the ssp signal at the dangling bond frequency region mainly stems from OH bonds nearly perpendicular to the surface.

As a comment on this discrepancy about the dangling OH direction, we should point out that a OH bond considerably tilted from the surface normal can still have substantial ssp component of hyperpolarizability, due to the large and nonzero components of $\partial \alpha_{zz} / \partial r_1$ and $\partial \mu_x / \partial r_1$ in the body-fixed frame. As we see in Table 1, significant nonzero components of the dipole/polarizability derivatives are $\partial \mu_z / \partial r_1 (\equiv \mu'_z)$, μ'_x , α'_{zz} , α'_{xx} , and α'_{yy} in the body-fixed frame of Fig. 1(a). We will consider some extreme cases of OH directions for simplicity, and two typical orientations of the surface OH bond are depicted in Fig. 11(d): perpendicular and parallel to the surface. In either case, some nonzero contribution to the ssp susceptibility appears with the local OH stretching while there is no significant contribution for sps . The previous analysis in Ref. [42], based on the intensity ratio of the ssp and sps signals, has led to a different conclusion on the OH orientation because the contribution of $\partial \mu_x / \partial r_1$ was neglected as were the tilted dangling bonds.

Fig. 11(b), the two-dimensional decomposition of the *ssp* susceptibility in the hydrogen-bonded region, exhibits quite different features. The existence of both positive and negative regions in Fig. 11(b) implies substantial cancellation in the average, leaving some net negative component in this frequency region. The most important *negative* contribution comes from the orientation about $\theta \sim 120^\circ$ ($\cos \theta \sim -0.5$) and $\phi \sim 90^\circ$, implying that both OH bonds point inwards towards the bulk, as schematically shown in Fig. 11(c).

5. Characterization of OH stretching modes

As discussed above, the SFG spectrum exhibits two distinct bands, assigned as hydrogen bonds and dangling bonds, but the characters of those vibrational modes have not been fully elucidated. Thus, our remaining goal is to characterize the OH stretching bands in the SFG spectrum using the results of the MD simulations.

As discussed in Section 2.2, the vibrational states consist of two kinds of eigenstates, as Eq. (8) gives two eigenstates for a water molecule. The two vibrational manifolds give opposite contributions to the susceptibility χ_{ssp}^r as demonstrated in Fig. 12, where the two vibrational manifolds have opposite signs in the imaginary part and little overlap in frequency range. Note that the lower/higher components do not necessarily correspond to the symmetric/antisymmetric OH stretching but can take on some local-mode character in an asymmetric environment, where $\omega_1 \neq \omega_2$ in Eq. (8).

5.1. Symmetric/antisymmetric mode character

The mode character ranging between symmetric and antisymmetric OH stretching is conveniently represented by an index $2C_1C_2$, where C_1, C_2 are the coefficients of the two local stretch components in Eq. (8) for the vibrational wave function. The index $2C_1C_2$ can be defined for each molecule: $2C_1C_2 = +1$ indicates a pure symmetric stretching mode and $2C_1C_2 = -1$ a pure antisymmetric mode. The statistical average $\langle 2C_1C_2 \rangle$ is shown in Fig. 13 as a function of frequency in both the bulk

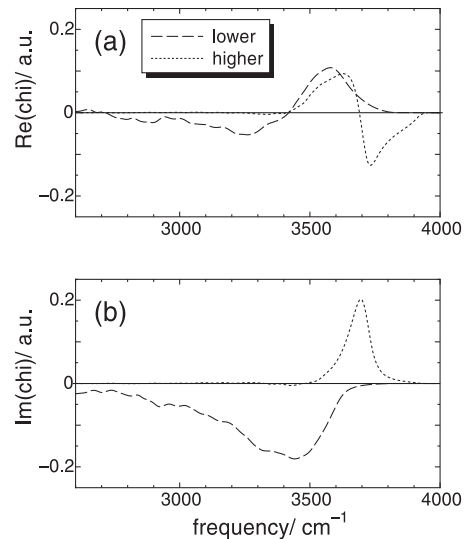


Fig. 12. Susceptibility χ_{ssp}^r per unit surface area decomposed into two vibrational eigenstates, lower energy state (---) and higher energy state (···). Panels (a) and (b) show the real and imaginary parts, respectively. Unit: a.u.

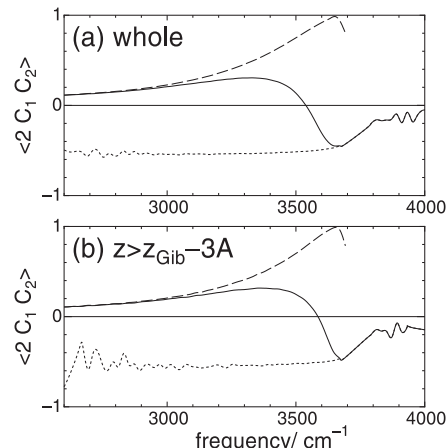


Fig. 13. Average mode character $\langle 2C_1C_2 \rangle$ as a function of frequency in the entire system (panel a) and in the first monolayer of surface (panel b). The solid lines denote the average over all eigenstates at each frequency. The dashed lines correspond to $\langle 2C_1C_2 \rangle_{\text{low}}$ averaged within the lower energy component of the eigenstates, and the dotted lines to $\langle 2C_1C_2 \rangle_{\text{high}}$ within the higher energy component.

and surface regions. In either region, the average mode character $\langle 2C_1C_2 \rangle$ exhibits a sinusoidal behavior, changing its sign at about 3600 cm^{-1} .

However, the index $\langle 2C_1C_2 \rangle_{\text{low}}$ averaged within the lower energy eigenstates (dashed line) is always positive, indicating net symmetric stretching character, while $\langle 2C_1C_2 \rangle_{\text{high}}$ within the higher energy eigenstates (dotted line) is always negative, indicating net antisymmetric stretching. The overall character $\langle 2C_1C_2 \rangle$ approaches $\langle 2C_1C_2 \rangle_{\text{low}}$ below 3300 cm^{-1} and $\langle 2C_1C_2 \rangle_{\text{high}}$ above 3700 cm^{-1} , but it *never* approaches either pure symmetric ($\sim +1$) or antisymmetric (~ -1) character in any frequency region. Fig. 13(a) and (b) show an overall similarity, though a transition occurs in the surface region at a somewhat higher frequency. It is noteworthy that the vibrational mode characters in terms of symmetric/antisymmetric stretching exhibit an essentially similar behavior in the frequency domain in the bulk and the surface.

5.2. Degree of mode delocalization

Next, we discuss the degree of delocalization in the OH stretching normal modes. Note that $\langle 2C_1C_2 \rangle \approx 0$ does not necessarily indicate that all vibrations are localized, since this vanishing might result from a inhomogeneous mixture of symmetric and antisymmetric modes. In order to assess the degree of mode delocalization, another index $\langle |2C_1C_2|^2 \rangle$, in the range 0–1, is introduced. $|2C_1C_2|^2 = 0$ indicates a completely localized OH stretching mode, and $|2C_1C_2|^2 = 1$ means a completely delocalized mode, either symmetric or antisymmetric. Fig. 14 shows a bell-shaped curve of the overall average $\langle |2C_1C_2|^2 \rangle$ with a maximum delocalization at about $3500\text{--}3600 \text{ cm}^{-1}$. The vibrational modes are clearly localized in both the tail regions (i.e. ~ 3000 and $\sim 4000 \text{ cm}^{-1}$). The frequency of the maximum delocalization about 3600 cm^{-1} is nearly located at the zero point $\langle 2C_1C_2 \rangle = 0$ of Fig. 13. This implies that the vibrational modes in the $3500\text{--}3600 \text{ cm}^{-1}$ region represent an inhomogeneous mixture of symmetric and antisymmetric characters. Fig. 14(a) and (b) also indicates a similarity of the mode delocalization character in the bulk and surface; any remarkable surface-specific features of the vibrational modes are not observed in either index $\langle 2C_1C_2 \rangle$ or $\langle |2C_1C_2|^2 \rangle$.

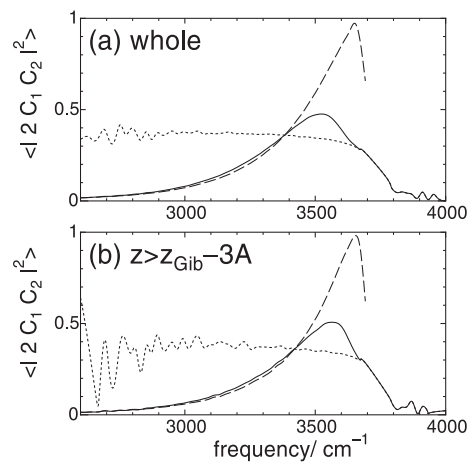


Fig. 14. Average degree of mode delocalization $\langle |2C_1C_2|^2 \rangle$ as a function of frequency in the whole system (panel a) and in the first monolayer of surface (panel b). The other notations are same as in Fig. 13.

5.3. Relevance to the SFG spectrum

The above results of Figs. 13 and 14 can be utilized for the assignment of the SFG spectral bands. As discussed in Section 4 and apparent in Fig. 7, the SFG spectrum of OH stretching frequency region consist of two bands. The vibrational modes in the dangling bond band $\sim 3700 \text{ cm}^{-1}$ are strongly localized, which is concordant with the concept that a water molecule has one dangling bond at the surface, though these modes have some antisymmetric stretching character.

In previous literature discussions, the assignment of the hydrogen-bonded band at $3000\text{--}3500 \text{ cm}^{-1}$ is less clear, but the band is often regarded as consisting of two subbands [38,42], centered at ~ 3200 and $\sim 3450 \text{ cm}^{-1}$, with the latter dominating the overall intensity. The former subband is distinct in the IR or Raman spectrum of ice [49,50], and the latter subband is distinct in liquid water [48]. On the basis of the IR and Raman spectra and a previous model of hydrogen bond effects represented by two kinds of (symmetric/antisymmetric) environments [84], Shultz and co-workers [38] suggested that the lower subband arises from the symmetric stretching in symmetric environments, and the higher subband from a mixture of symmetric stretching in symmetric environments and

antisymmetric stretching in asymmetric environments. The present analysis partly agrees with this assignment in the sense that the former subband frequency region $\sim 3200 \text{ cm}^{-1}$ takes on some symmetric stretching character and the latter frequency region $\sim 3450 \text{ cm}^{-1}$ is a mixture of symmetric and antisymmetric stretching characters. These are also consistent with the experimental frequency dependence of Raman depolarization ratio [85]. However, in the lower subband region, the vibrational modes are strongly localized, which is hardly compatible with the above assignment, since Eq. (8) implies that a symmetric environment would result in a delocalized character in general. In the higher subband region, Figs. 13 and 14 show that the two eigenstate components (represented by dashed and dotted lines) acquire considerable symmetric and antisymmetric stretching characters, respectively, and both the symmetric and antisymmetric stretching modes are delocalized to the same extent. Our simulation results thus indicate a limitation of interpretations based on two distinct symmetric/antisymmetric environments.

6. Concluding remarks

SFG spectroscopy provides an experimentally unique way to explore microscopic liquid interfaces. However, its theoretical analysis has been hindered so far by a lack of the information on molecular hyperpolarizability tensors and their dependence on molecular vibrations. The present study provides a theoretical analysis of the SFG spectrum of water using ab initio calculations and MD simulations.

The essential features of the spectrum were reproduced and interpreted by resorting to an approximate modeling of the molecular vibrations, thus circumventing their explicit simulation. First, we used the $\text{Cl}^- \cdot (\text{H}_2\text{O})_2$ model cluster to derive a theoretical expression of the molecular hyperpolarizability of a water molecule in the OH stretching frequency region. The normal modes of water OH stretching vibrations, their frequency shifts, and the environmental influence on the vibrational coupling and the hyperpolarizability were formulated and thoroughly tested (Figs. 2–

4), in forms readily applicable in the MD simulations.

Then, the water SFG spectrum was simulated from the surface structures generated via MD simulations (Fig. 5). The simulated SFG spectrum reproduces the essential experimental features quite well (Fig. 6), and the *sps* signal was predicted to be much weaker than *ssp*, particularly in the high-frequency dangling bond region ($\sim 3700 \text{ cm}^{-1}$, cf. Fig. 7). The dangling bond band was found to be sensitive exclusively to the surface top monolayer structure, while the hydrogen-bonded band ($3000\text{--}3500 \text{ cm}^{-1}$) reflects the structure of a few top monolayers (Fig. 8). The dangling and hydrogen-bonded bands have opposite signs of imaginary susceptibility, which indicate different OH orientations at the surface (Fig. 9). The two bands stem from quite different molecular orientations at the surface, and tilted OH dangling bonds are rather important to the SFG signal in the dangling bond region (Figs. 10 and 11). It was found that 21% of the surface OH bonds positively contribute to the dangling bond signal.

Further, we assigned the OH stretching modes in the SFG spectrum. Vibrational modes below 3600 cm^{-1} have overall symmetric stretching character, whereas those above 3600 cm^{-1} have overall antisymmetric character (Fig. 13). The transition region ($\sim 3600 \text{ cm}^{-1}$) consists of an inhomogeneous mixture of symmetric and antisymmetric modes, while in both the tail frequency regions (~ 3000 and $\sim 4000 \text{ cm}^{-1}$) the modes approach localized OH stretching character (Fig. 14). The frequency dependence of these normal mode features is similar in both the surface and the bulk.

Finally, we point out some future directions for extension of our study. The present study can be extended via a more rigorous ab initio treatment of the molecular hyperpolarizability, e.g. by including its nonresonant components and its dependence on environmental perturbations, which would likely improve on our current description of the hydrogen-bonded band sub-structure, sometimes experimentally seen [38,42] but not clearly apparent in the simulated SFG spectrum. Another extension would involve the inclusion of intra- and intermolecular vibrational couplings beyond the

coupling of the two local water OH stretches treated here via a flexible molecular model.

The motivation behind this study is the application of the simulation methodologies to description of atmospherically relevant aqueous solutions and interfaces. Our group is currently involved in the modeling of the microscopic surface structures of ice and sulfuric/nitric acid aqueous solutions (Morita and Hynes, work in progress) to explore heterogeneous reactions mechanisms in the atmosphere (Bianco and Hynes, work in progress).

Acknowledgements

This work was supported in part by NSF grants ATM-9613802, CHE-9700419, and CHE-9709195. The computations were mainly performed using the Molecular Science Computing Facility (MSCF) in the William R. Wiley Environmental Molecular Sciences Laboratory at the Pacific Northwest National Laboratory. The MSCF is funded by the Office of Biological and Environmental Research in the US Department of Energy. Pacific Northwest is operated by Battelle for the US Department of Energy under Contract DE-AC06-76RLO 1830. The authors are grateful to Prof. David Jonas and Dr. W.H. Thompson for valuable discussions and Dr. R. Bianco for careful reading of the manuscript. A.M. thanks Prof. S. Kato for his encouragement.

References

- [1] A.W. Adamson, *Physical Chemistry of Surfaces*, fifth ed., Wiley, New York, 1990.
- [2] C.A. Croxton (Ed.), *Fluid interfacial phenomena*, Wiley, New York, 1986.
- [3] I. Benjamin, *Acc. Chem. Res.* 28 (1995) 233.
- [4] I. Benjamin, *Chem. Rev.* 96 (1996) 1449.
- [5] K.B. Eisenthal, *Chem. Rev.* 96 (1996) 1343.
- [6] K.B. Eisenthal, *Ann. Rev. Phys. Chem.* 43 (1992) 627.
- [7] R.M. Corn, D.A. Higgins, *Chem. Rev.* 94 (1994) 107.
- [8] G.M. Nathanson, P. Davidovits, D.R. Worsnop, C.E. Kolb, *J. Phys. Chem.* 100 (1996) 13007.
- [9] P. Davidovits, J.H. Hu, D.R. Worsnop, M.S. Zahniser, C.E. Kolb, *Faraday Discuss.* 100 (1995) 65.
- [10] J.H. Seinfeld, S.N. Pandis, *Atmospheric chemistry and physics*, Wiley, New York, 1998.
- [11] S. Solomon, *Rev. Geophys.* 37 (1999) 275.
- [12] C.E. Kolb, D.R. Worsnop, M.S. Zahniser, P. Davidovits, L.F. Keyser, M.T. Leu, M.J. Molina, D.R. Hanson, A.R. Ravishankara, in: J.R. Barker (Ed.), *Progress and Problems in Atmospheric Chemistry*, World Scientific, Singapore, 1995, p. 771 (Chapter 18).
- [13] T. Peter, *Ann. Rev. Phys. Chem.* 48 (1997) 785.
- [14] R. Sander, *Surv. Geophys.* 20 (1999) 1.
- [15] G.N. Robinson, D.R. Worsnop, J.T. Jayne, C.E. Kolb, P. Davidovits, *J. Geophys. Res.* 102 (1997) 3583.
- [16] J.H. Hu, J.P.D. Abbatt, *J. Phys. Chem. A* 101 (1997) 871.
- [17] G.C.G. Waschewsky, J.P.D. Abbatt, *J. Phys. Chem. A* 103 (1999) 5312.
- [18] D.R. Hanson, A.R. Ravishankara, *J. Phys. Chem.* 98 (1994) 5728.
- [19] D.J. Donaldson, A.R. Ravishankara, D.R. Hanson, *J. Phys. Chem. A* 101 (1997) 4717.
- [20] D.J. Donaldson, *J. Phys. Chem. A* 103 (1999) 62.
- [21] R. Vogt, C. Elliott, H.C. Allen, J.M. Laux, J.C. Hemminger, B.J. Finlayson-Pitts, *Atmos. Environ.* 30 (1996) 1729.
- [22] G.A. Somorjai, *Introduction to surface chemistry and catalysis*, Wiley, New York, 1994.
- [23] R.M. Townsend, J. Gryko, S.A. Rice, *J. Chem. Phys.* 82 (1985) 4391.
- [24] R.M. Townsend, S.A. Rice, *J. Chem. Phys.* 94 (1991) 2207.
- [25] M.A. Wilson, A. Pohorille, L.R. Pratt, *J. Phys. Chem.* 91 (1987) 4873.
- [26] M.A. Wilson, A. Pohorille, L.R. Pratt, *J. Chem. Phys.* 90 (1989) 5211.
- [27] M. Matsumoto, Y. Kataoka, *J. Chem. Phys.* 88 (1988) 3233.
- [28] K.A. Motakabbir, M.L. Berkowitz, *Chem. Phys. Lett.* 176 (1991) 61.
- [29] I. Benjamin, *Phys. Rev. Lett.* 73 (1994) 2083.
- [30] R.S. Taylor, L.X. Dang, B.C. Garrett, *J. Phys. Chem.* 100 (1996) 11720.
- [31] V.P. Sokhan, D.J. Tildesley, *Mol. Phys.* 92 (1997) 625.
- [32] Y.R. Shen, *Surface spectroscopy by nonlinear optics*, in: T.W. Hansch, M. Inguscio (Eds.), *Proc. Int. School of Physics, 'Enrico Fermi'*, vol. CXX, North Holland, Amsterdam, 1994, p. 139.
- [33] A. Tadjeddine, A. Peremans, *Surf. Sci.* 368 (1996) 377.
- [34] P.B. Miranda, Y.R. Shen, *J. Phys. Chem. B* 103 (1999) 3292.
- [35] R. Superfine, J.Y. Huang, Y.R. Shen, *Phys. Rev. Lett.* 66 (1991) 1066.
- [36] C. Hirose, H. Yamamoto, N. Akamatsu, K. Domen, *J. Phys. Chem.* 97 (1993) 10064.
- [37] D. Zhang, J. Gutow, K.B. Eisenthal, *J. Phys. Chem.* 98 (1994) 13729.
- [38] S. Baldelli, C. Schnitzer, M.J. Shultz, D.J. Campbell, *J. Phys. Chem. B* 101 (1997) 10435.
- [39] S. Baldelli, C. Schnitzer, D.J. Campbell, M.J. Shultz, *J. Phys. Chem. B* 103 (1999) 2789.
- [40] C. Schnitzer, S. Baldelli, M.J. Shultz, *J. Phys. Chem. B* 104 (2000) 585.

- [41] Y.R. Shen, Principle of nonlinear optics, Wiley, New York, 1984.
- [42] Q. Du, R. Superfine, E. Freysz, Y.R. Shen, Phys. Rev. Lett. 70 (1993) 2313.
- [43] K.L. Vodopyanov, Sov. Phys. JETP 70 (1990) 114.
- [44] D.W. Oxtoby, Adv. Chem. Phys. 40 (1978) 1.
- [45] D.E. Woon, T.H. Dunning Jr., J. Chem. Phys. 100 (1994) 2975.
- [46] M.H. Brooker, G. Hancock, B.C. Rice, J. Shapter, J. Raman Spectr. 20 (1989) 683.
- [47] M. Oki, et al. (Ed.), *Kagaku Binran*, fourth ed., Maruzen, Tokyo, 1993 (in Japanese).
- [48] G.E. Whalraten, J. Chem. Phys. 47 (1967) 114.
- [49] J.E. Bertie, E. Whalley, J. Chem. Phys. 40 (1964) 1637.
- [50] J.E. Bertie, H.J. Labbè, E. Whalley, J. Chem. Phys. 50 (1969) 4501.
- [51] M.G. Sceats, S.A. Rice, J. Chem. Phys. 71 (1979) 973.
- [52] M.G. Sceats, M. Stavola, S.A. Rice, J. Chem. Phys. 71 (1979) 983.
- [53] J.R. Reimers, R.O. Watts, Chem. Phys. 85 (1984) 83.
- [54] W.H. Thompson, J.T. Hynes, J. Am. Chem. Soc., in press.
- [55] R. Rey, J.T. Hynes, J. Chem. Phys. 108 (1998) 142.
- [56] M. Cho, G.R. Fleming, S. Saito, I. Ohmine, R.M. Stratt, J. Chem. Phys. 100 (1994) 6672.
- [57] M.J. Frisch, G.W. Trucks, H.B. Schlegel, G.E. Scuseria, M.A. Robb, J.R. Cheeseman, V.G. Zakrzewski, J.A. Montgomery, R.E. Stratmann, J.C. Burant, S. Dapprich, J.M. Millam, A.D. Daniels, K.N. Kudin, M.C. Strain, O. Farkas, J. Tomasi, V. Barone, M. Cossi, R. Cammi, B. Mennucci, C. Pomelli, C. Adamo, S. Clifford, J. Ochterski, G.A. Petersson, P.Y. Ayala, Q. Cui, K. Morokuma, D.K. Malick, A.D. Rabuck, K. Raghavachari, J.B. Foresman, J. Cioslowski, J.V. Ortiz, B.B. Stefanov, G. Liu, A. Liashenko, P. Piskorz, I. Komaromi, R. Gomperts, R.L. Martin, D.J. Fox, T. Keith, M.A. Al-Laham, C.Y. Peng, A. Nanayakkara, C. Gonzalez, M. Challacombe, P.M.W. Gill, B.G. Johnson, W. Chen, M.W. Wong, J.L. Andres, M. Head-Gordon, E.S. Replogle, J.A. Pople, *GAUSSIAN 98* (Revision A.6) Gaussian, Pittsburgh, PA, 1998.
- [58] A.D. Becke, J. Chem. Phys. 98 (1993) 5648.
- [59] C. Lee, W. Yang, R.G. Parr, Phys. Rev. B 37 (1988) 785.
- [60] A. Morita, S. Kato, J. Chem. Phys. 110 (1999) 11987.
- [61] W.F. Murphy, Mol. Phys. 36 (1978) 727.
- [62] P.W. Atkins, *Physical Chemistry*, fifth ed., W.H. Freeman, New York, 1994, p. 584.
- [63] D.A. Long, Raman spectroscopy, McGraw-Hill, New York, 1977.
- [64] P. Ayotte, G.H. Weddle, J. Kim, M.A. Johnson, J. Am. Chem. Soc. 120 (1998) 12361.
- [65] J.H. Choi, K.T. Kuwata, Y.B. Cao, M. Okumura, J. Phys. Chem. A 102 (1998) 503.
- [66] H.E. Dorsett, R.O. Watts, S.S. Xantheas, J. Phys. Chem. A 103 (1999) 3351.
- [67] S.S. Xantheas, J. Phys. Chem. 100 (1996) 9703.
- [68] X.G. Zhao, A. Gonzalez-Lafont, D.G. Truhlar, R. Stedler, J. Chem. Phys. 94 (1991) 5544.
- [69] J.E. Combariza, N.R. Kestner, J. Jortner, J. Chem. Phys. 100 (1994) 2851.
- [70] F. Huisken, M. Kaloudis, A. Kulcke, J. Chem. Phys. 104 (1996) 17.
- [71] T.R. Dyke, J.S. Muenter, J. Chem. Phys. 60 (1974) 2929.
- [72] H.J.C. Berendsen, J.R. Grigera, T.P. Straatsma, J. Phys. Chem. 91 (1987) 6269.
- [73] H.J. Strauch, P.T. Cummings, J. Chem. Phys. 96 (1992) 864.
- [74] D.F. Coker, R.E. Miller, R.O. Watts, J. Chem. Phys. 82 (1985) 3554.
- [75] E.B. Wilson Jr., J.C. Decius, P.C. Cross, *Molecular Vibrations*, McGraw-Hill, New York, 1955.
- [76] C.M. Huggins, G.C. Pimentel, J. Phys. Chem. 60 (1956) 1615.
- [77] G.C. Pimentel, A.L. McClellan, *The hydrogen bond*, W.H. Freeman, San Francisco, 1960 (Chapter 3).
- [78] M.P. Allen, D.J. Tildesley, *Computer simulation of liquids*, Oxford University Press, New York, 1991.
- [79] G.M. Torrie, J.P. Valleau, J. Chem. Phys. 73 (1980) 5807.
- [80] J.P. Valleau, A.A. Gardner, J. Chem. Phys. 86 (1987) 4162.
- [81] K. Kinoshita, H. Yokota, J. Phys. Soc. Jpn. 20 (1965) 1086.
- [82] A. Braslav, M. Deutsch, P.S. Pershan, A.H. Weiss, J. Als-Nielsen, J. Bohr, Phys. Rev. Lett. 54 (1985) 114.
- [83] A. Braslav, P.S. Pershan, G. Swislow, B.M. Ocko, J. Als-Nielsen, Phys. Rev. A 38 (1988) 2457.
- [84] J.R. Scherer, M.K. Go, S. Kint, J. Phys. Chem. 78 (1974) 1304.
- [85] K. Cunningham, P.A. Lyons, J. Chem. Phys. 59 (1973) 2132.
- [86] D.E. Gragson, G.L. Richmond, J. Phys. Chem. B 102 (1998) 3847.
- [87] D.E. Gragson, B.M. McCarty, G.L. Richmond, J. Am. Chem. Soc. 119 (1997) 6144.